sciendo Applied Mathematics and Nonlinear Sciences, 9(1) (2024) 1-20

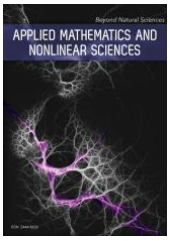

Applied Mathematics and Nonlinear Sciences

https://www.sciendo.com

Visualization Challenges of Virtual Reality 3D Images in New Media Environments

Yige Sun[1], Zixuan Zhang[1], Nan Yan[1,†]

1. HBU-UCLan School of Media, Communication and Creative Industries, Hebei University, Baoding, Hebei, 071000, China.

Submission Info

Communicated by Z. Sabir
Received March 24, 2024
Accepted June 11, 2024
Available online July 9, 2024

Abstract

This paper proposes a three-dimensional image visualization process to face-drawing three-dimensional image reconstruction algorithm to obtain the data field with three-dimensional space, using color adjustment based on global color correction and local Poisson fusion to optimize the splicing seams between the texture color blocks and updating the visualization technology of three-dimensional images. Divide the digital display design and create a virtual reality visualization display using 3D modeling in combination with the new media environment. Propose design steps to visualize virtual reality three-dimensional images in the new media environment by combining the key algorithms of three-dimensional image visualization from the previous section. Combined with the application of new media displaying 3D images, the concept of artifact shape in reconstructed images is proposed to analyze the quality of 3D image reconstruction by taking the Herman model and Sheep-Logan model as the research object. Test experiments are conducted to examine the visual impact of texture mapping algorithms, and different sampling intervals are set to measure the drawing time of 3D reconstruction. For the data size and number of pictures of other organizations, the processing time of the 3D image reconstruction algorithm based on surface drawing is no more than 2s. The denser the sampling points are, the higher the degree of fitting, the more complete the preservation of isosurface information is, the finer the effect of 3D reconstruction, and the higher the quality of the image.

Keywords: Three-dimensional image reconstruction; Virtual reality; Texture mapping algorithm; Visualization technology.
AMS 2010 codes: 97P20

†Corresponding author.
Email address: ynanhbu@163.com

ISSN 2444-8656
https://doi.org/10.2478/amns-2024-1785

1 Introduction

In the past decade, with the continuous improvement of the computing performance of devices, virtual reality technology has been developed rapidly [1]. Virtual reality technology not only brings three-dimensional simulation of visual perception for human beings but also can bring simulation of feelings in hearing, touch, smell, and other aspects [2-3]. Image-based 3D reconstruction algorithm is the key technology of virtual reality technology and a hot direction of recent research, which can improve the user experience and enhance the efficiency of human-computer interaction [4-5].

Three-dimensional image reconstruction belongs to the field of computer vision; the image has irregularity, and it is easy to be interfered with by noise in the reconstruction process, so three-dimensional image reconstruction has greater difficulty [6-7]. The traditional digital holography method applied to three-dimensional image reconstruction utilizes the drawing method of the graphic feature body to obtain the coefficient point cloud in the digital holographic image to realize the three-dimensional reconstruction of the image [8-9]. Although the 3D image reconstructed by the digital holography method has better smoothness, the computational process is complicated, it is easy to be interfered with by the outside world, and it has poor robustness [10]. In addition, the 3D image reconstruction method of active polarization imaging extracts image features with a high degree of similarity to the target shape by constructing a reconstruction template shape and realizes 3D image reconstruction by using the deformation displacement vector compensation method [11-12]. Although the dynamic polarization imaging method takes less time, the statistical information expression ability of the reconstructed image is poor, and the clarity is low [13]. Compared with traditional 3D image reconstruction, visualization reconstruction using virtual reality technology can display the internal information of the image more clearly and improve the ability to express the statistical data of the image [14-16].

Literature [17] proposed a virtual reality-based 3D image reconstruction method to detect 3D morphological features of marine plankton, which firstly utilizes two cameras to collect image data from different angles, then calculates the deviation of the image feature points based on the stereo matching results, and operates the principle of triangle similarity to mine the depth information. Literature [18] in the high-resolution 3D object reconstruction study found that by incorporating an edge computing framework, 3D reconstruction based on deep learning can realize intelligent processing of edges. Literature [19] Based on a multi-camera capture system with a modular setup for high-quality 3D reconstruction of dynamic real-world objects, its proposed algorithm obtains the most realistic natural representation. It is easily integrated with augmented display and virtual reality applications. Literature [20] addresses the 3D point cloud alignment problem by applying the method of local angular statistical histograms to form a description of the local geometry, which is augmented by an algorithm that first detects the triangular matching points and aggregates them into a set of matching points, and then calculates multiple transformations between the two point clouds, and finally determines the optimal transformations by using the error function. Literature [21] developed an end-to-end shape-aware scatter matching network incorporating shape mask information in order to improve the accuracy and completeness of parallax computation in cross-domain applications, and the learning algorithm makes it possible to still have high sample accuracy in different cross-domain scenarios. Literature [22] based on multi-view object 3D reconstruction neural network realizes the smooth conversion of object modeling from 2D to 3D features. It is able to accurately recover the 3D features of the object by 2D features, which improves the performance of single-view reconstruction. Literature [23] adopts a mesh motion statistical feature matching algorithm to obtain highly accurate 3D model reconstruction in low texture scenes, which determines whether the matching is correct or not by calculating the number of matching points in the neighborhood.

This paper proposes a voxel-based face-drawn method for reconstructing 3D images, which treats the 3D image as a sampling result of a 3D discrete data field and extracts step-edge surfaces using a gradient function. Propose a texture mapping algorithm to remove irrelevant files, reduce the number of faces in the model, and update the 3D image visualization. Design the steps for virtual reality visualization display based on 3D modeling, combine new media application data, and propose metrics for assessing image quality. Herman model and Sheep-Logan model are selected as research objects to evaluate the reconstructed image quality of the 3D image reconstruction algorithm based on face drawing, statistically calculate the preprocessing time for human image reconstruction under different data sizes, calculate the time required for 3D reconstruction under different sampling intervals, and detect the quality of visualization display of 3D images in the new media environment.

2 Three-dimensional image visualization techniques

2.1 3D Visualization Process

1) Some basic concepts in 3D visualization, such as body data and voxels.

Body data can be defined as a sampling function in a discrete bounded 3D space. This kind of voxel data is said to be regularly structured if the sampling is regularly structured. In most cases, the voxel data is regularly structured, i.e., the sampling is uniform in all three directions of the space. This data is described as a three-dimensional discrete image and can be depicted as:

$$f\left(x,y,z\right),Which\begin{cases} x=x_1,x_2,\cdots,x_i; & \left(x_i-x_{i-1}=\Delta x\right) \\ y=y_1,y_2,\cdots,y_n; & \left(y_i-y_{i-1}=\Delta y\right) \\ z=z_1,z_2,\cdots,z_n; & \left(z_i-z_{i-1}=\Delta z\right) \end{cases} \tag{1}$$

Sampling Points and Sampling Values A sampling point is the spatial location of a sample. The sample value is a quantized value of some physical property of the substance at the sampling point. For example, in a CT image, the sampling value represents the degree of absorption of X light by the substance.

A voxel is defined as a small rectangular region. Its length, width, and height are the sampling spacing in each of the three directions.

2) The process of 3D visualization is shown in Fig. 1, where a real object/computer model is used to obtain the voxel data, and a 2D display image with 3D realism is drawn using 3D digital image segmentation technology voxels.

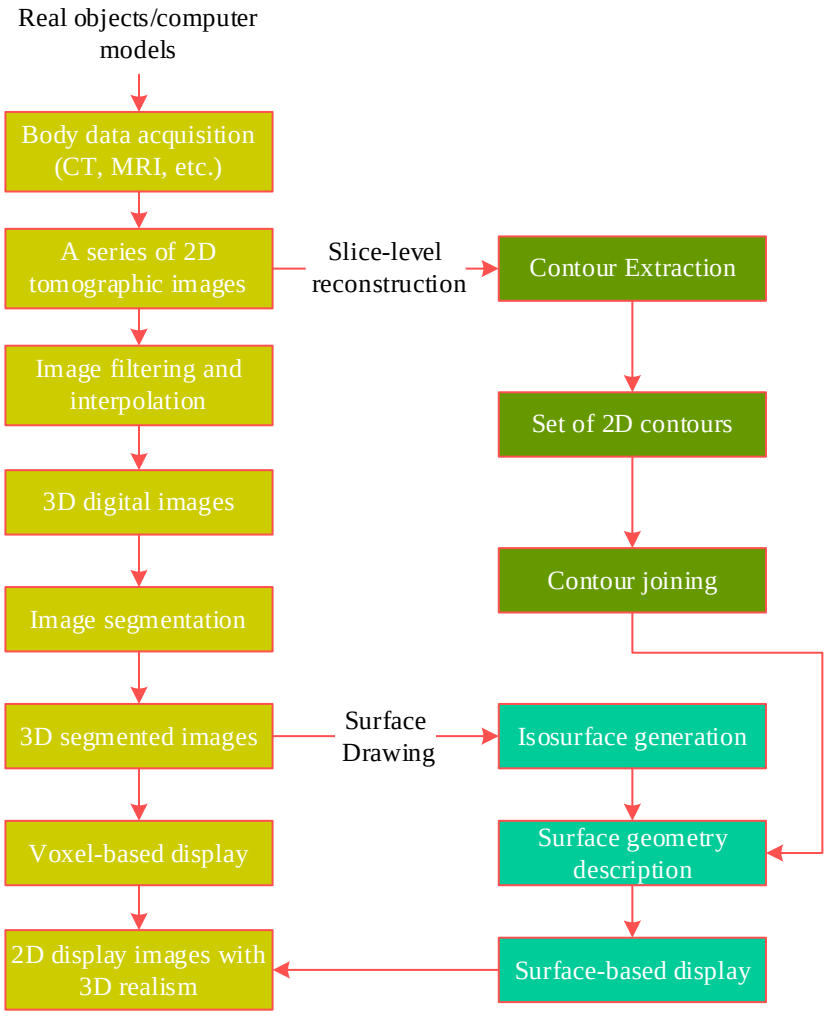

Figure 1. Three-dimensional visualization process

2.2 Key algorithms for visualization

2.2.1 3D Image Reconstruction

Two-dimensional images are not able to be displayed directly and intuitively on a computer screen, unlike two-dimensional images. The use of visualization techniques to image three-dimensional photos results in a two-dimensional visual image that has a three-dimensional stereo sense and reflects the two-dimensional structure [24-26].

There are two methods to obtain a data field with three-dimensional space: body plotting and face plotting. The main topic of this paper is the face drawing algorithm.

1) Face drawing method on voxels

The equivalent face extraction algorithm deals with data that are three-dimensional orthogonal data fields, which the following equation can describe:

$$F_{i,jk} = F\left(x_i, y_j, z_k\right)\left(i = 1, \cdots, N_x j = i = 1, \cdots, N_y k = 1, \cdots, N_z\right) \tag{2}$$

The three-dimensional image can be viewed as a three-dimensional continuous function $f(x,y,z)$ that is sampled in a three-dimensional orthogonal data field as a result of spatially sampling the number of draws $S(x,y,z)$ that are ideally δ -pulse arrays, sampled at a distance of $\Delta x, \Delta y, \Delta z$:

$$S(x,y,z)=\sum_{i=-\infty}^{\infty}\sum_{j=-x}^{\infty}\sum_{k=-\infty}^{\infty}\delta\left(x-i\Delta x, y-i\Delta y, z-i\Delta z\right) \tag{3}$$

Among them:

$$\delta(x,y,z)=\begin{cases}1 & x,y,z=0\\ 0 & Other\end{cases} \tag{4}$$

The image obtained is:

$$f_D(i,j,k)=f(x,y,z)\delta\left(x-i\Delta x, y-i\Delta y, z-i\Delta z\right) \tag{5}$$

That is, the data is in three dimensions.

The three-dimensional empty data field can be regarded as a cube formed by a regular grid, in which 8 neighboring grid points form a small cubic structure, here called voxel structure, and 8 sampling points are vertices. The stored small cubes form a continuous sampled data field in 3D space. The voxel structure is shown in Fig. 2.

The coordinates of the 8 vertices of the voxel are (i,j,k), $(i+1,j,k)$, $(i,j+1,k)$, $(i,j,k+1)$, $(i+1,j+1,k)$, $(i+1,j,k+1)$, $(i,j+1,k+1)$ and $(i+1,j+1,k+1)$, so any point within the voxel can be interpolated by these 8 vertices. For example, if a point $t(x,y,z)$ in the voxel has two field coordinates $v_0(x_0,y_0,z_0)$ and $v_7(x_1,y_1,z_1)$, then the gray value of t can be calculated by the following formula:

$$\begin{aligned}t=&\frac{x_1-x}{\Delta x}*\frac{y-y_0}{\Delta y}*\frac{z_1-z}{\Delta z}*v_0+\frac{x_1-x}{\Delta x}*\frac{y_1-y'}{\Delta y}*\frac{z_1-z}{\Delta z}*v_1\\&+\frac{x-x_0}{\Delta x}*\frac{y_1-y'}{\Delta y}*\frac{z_1-z}{\Delta z}*v_2+\frac{x-x_0}{\Delta x}*\frac{y-y_0}{\Delta y}*\frac{z_1-z}{\Delta z}*v_3\\&+\frac{x_1-x}{\Delta x}*\frac{y-y_0}{\Delta y}*\frac{z-z_0}{\Delta z}*v_4+\frac{x_1-x}{\Delta x}*\frac{y_1-y_1}{\Delta y}*\frac{z-z_0}{\Delta z}*v_5\\&+\frac{x-x_0}{\Delta x}*\frac{y_1-y}{\Delta y}*\frac{z-z_0}{\Delta z}*v_6+\frac{x-x_0}{\Delta x}*\frac{y-y_0}{\Delta y}*\frac{z-z_0}{\Delta z}*v_7\end{aligned} \tag{6}$$

It is obtained by organizing the formulas:

$$t(x,y,z)=a_0+a_1x+a_2y+a_3z+a_4xy+a_5yz+a_6xz+a_7xyz \tag{7}$$

Where $a_0 \sim a_7$ is a constant determined by the coordinates and gray values of the 8 vertices.

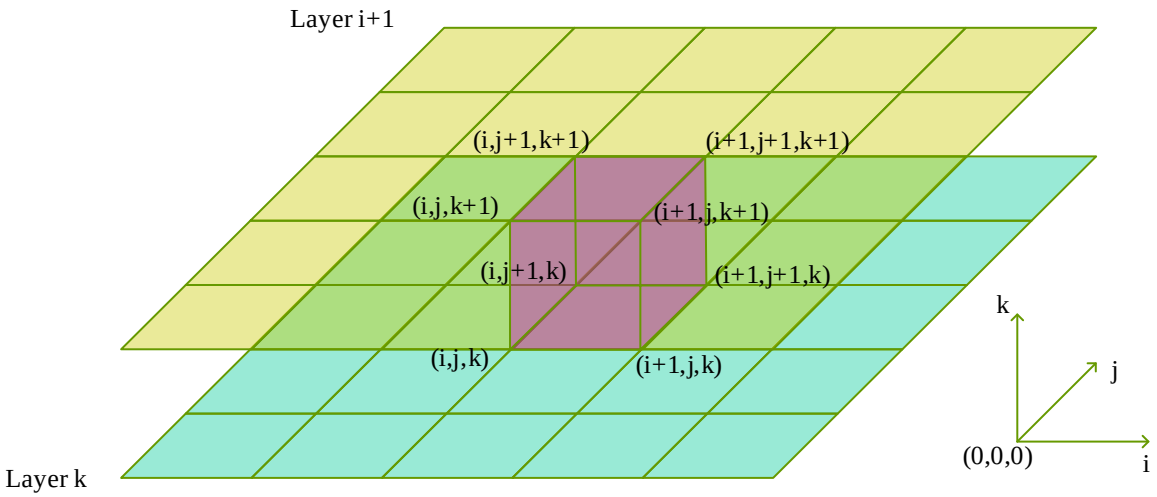

Figure 2. Body structure

From the voxel structure, the spatial data field can be regarded as a collection of sampling points about a certain physical property in a certain spatial region, and the values of the non-sampling points are obtained by interpolation of their neighboring sampling points, so the collection of all the points equal to a certain selected value within this spatial data field is defined as an equivariant surface, and due to the fact that different substances have different attributes, the equivariant surface can be expressed as a junction of various substances, that is a The surface of a substance.

An isosurface is a surface in a spatial data field that encompasses all points with the same gray value in three dimensions and can be described as:

$$\left\{(x,y)\middle| f(x,y,z)=d\right\} \tag{8}$$

Where d denotes the size of the equivalence.

However, not all voxels have equivalent surfaces, only when the voxel's 8 vertices exist both less than C points and more than C points, such voxels have equivalent surfaces, on the contrary, all 8 vertices are greater than C or less than C, there is no equivalent surface inside the voxel. Here, let $f\left(x_i,y_j,z_k\right)=c$ be an equivariant point, $f\left(x_i,y_j,z_k\right)\geq c$ be a positive point, and $f\left(x_i,y_j,z_k\right)\leq c$ be a negative point.

There are two general methods of calculating the value of the equivalence surface, the calculation of the value of the value of the value of the value of the gray scale and the calculation of the value of the value of the value of the value of the value of the distance. Define $d(x,y,z)$ as the continuous hermitian surface of a three-dimensional image $f(x,y,z)$, and $I(r)$ as the equivalence surface of $f(x,y,z)$, whose value is equal to r.

To determine the value of the equivalence surface using the gray value, the value of the smallest sum of the squares of the differences between the equivalence r and the gray values of all points on the continuous hidden surface $d(x,y,z)$ is calculated as follows:

$$\min_r \iint \left[f(x,y,z) - r \right]^2 dS, r \in (0,\infty) \tag{9}$$

By mathematical principles, the value of r is obtained when the derivative equals 0.

Here make $F(r) = \min_r \int f(x,y,z) - r \Big]^2 dS$, and the value of r at $F'(r) = 0$.

Simplifying the formula gives:

$$r = \frac{\int_{d(x,y,z)} f(x,y,z) dS}{\int dS} \tag{10}$$

From the above equation, the average gray value of all points on the continuous hidden surface $d(x,y,z)$ is the value of this equivalent surface.

2) Extraction of stepped edge surface

This paper defines the 3D image as the result of sampling a 3D discrete data field. Eight adjacent grid points form a voxel structure, and all voxels are combined into a continuous sampling region of the 3D image data. Therefore, the 3D image can be represented as a 3D concatenated function $f(x,y,z)$, and then the partial differentials can be derived $f(x,y,z)$ along the direction of X,Y,Z the three coordinate axes, respectively:

$$\frac{\partial f}{\partial x}, \frac{\partial f}{\partial y}, \frac{\partial f}{\partial z} \tag{11}$$

The Laplacian function for $f(x,y,z)$ is $\nabla^2 f(x,y,z)$. The gradient function for $f(x,y,z)$ is $\nabla f(x,y,z)$. Then the Laplacian function for $f(x,y,z)$ is as follows:

$$\nabla^2 f(x,y,z) = \frac{\partial^2 f}{\partial x^2} + \frac{\partial^2 f}{\partial y^2} + \frac{\partial^2 f}{\partial z^2} \tag{12}$$

The formula for its gradient function is as follows:

$$\left\| \nabla^2 f(x,y,z) \right\| = \sqrt{\left(\frac{\partial f}{\partial x} \right)^2 + \left(\frac{\partial f}{\partial y} \right)^2 + \left(\frac{\partial f}{\partial z} \right)^2} \tag{13}$$

Where $f(\dot{x},y,z)$ contains a stepped edge surface described as follows:

$$\begin{cases} \nabla^2 f(x,y,z) = 0 \\ \left\| \nabla f(x,y,z) \right\| \geq T \end{cases} \tag{14}$$

T is a set gradient threshold, and this value is taken in the same way as this value of the gradient is taken in the same way as in the edge detection algorithm. This means that a stepped edge surface

needs to be an equivalent surface where the Laplace function of special $\left(\left\|\nabla f\left(x,y,z\right)\right\|\geq T\right)$ is zero. Thus a zero Laplace function is not necessarily an edge surface. Typically, stepped edge surfaces do not pass through the mesh vertices of a 3D image, but between neighboring mesh points. Then the points on the stepped edge surface $\nabla^2 f(x,y,z)=0$ lie between two neighboring network points whose Laplace function values are of opposite sign and the gradient values of the neighboring network points should be greater than the gradient threshold T. The mathematical model is read:

$$\begin{cases} \nabla^2 f\left(x_1,y_1,z_1\right)*\nabla^2 f\left(x_2,y_2,z_2\right)<0 \\ \left\|\nabla f\left(x_1,y_1,z_1\right)\right\|+\left\|\nabla f\left(x_2,y_2,z_2\right)\right\|\geq 2T \end{cases} \tag{15}$$

In this case, the 3D image function is the result of discrete sampling from the continuous function $f(x,y,z)$. In fact, the exact analytic form of the continuous function $f(x,y,z)$ is not known, and the values of the gradient and Laplacian function at each of the points sought are obtained by differencing.

For example, the gradient vector at point (i,j,k) is:

$$\begin{cases} G_x(i,j,k)=f(i+1,j,k)-f(i-1,j,k) \\ G_y(i,j,k)=f(i,j+1,k)-f(i,j-1,k) \\ G_z(i,j,k)=f(i,j,k+1)-f(i,j,k-1) \end{cases} \tag{16}$$

That is, the gradient vector at point (i,j,k) is $\left\{G_x,G_y,G_z\right\}$, its magnitude value is $\sqrt{G_x^2+G_y^2+G_z^2}$, and the value of the Laplacian function at point (i,j,k) is:

$$L(i,j,k)=\sum_{(n,m,l)\in U_{18}} f\left(n,m,l\right)-18*f\left(i,j,k\right) \tag{17}$$

Here U_{18} denotes the 18-neighborhood of point (i,j,k):

$$\begin{aligned} U_{18}=&\left\{(n,m,l):|n-i|+|m-j|+|l-k|\right. \\ &\left.=2,|n-i|\leq 1,|m-j|\leq 1,|l-k|\leq 1\right\}-\left\{i,j,k\right\} \end{aligned} \tag{18}$$

2.2.2 Texture Mapping

Texture mapping is an important component of representing virtual environments. In a 3D virtual scene, texture mapping is not just about enhancing realism. To establish three-dimensional objects in the scene, it is crucial to significantly reduce the file size. In the current computer hardware and network environment, the three-dimensional generation of the scene file is often required to minimize the number of faces of the model for some complex models such as trees, flowers, and plants. The use of three-dimensional modeling is unrealistic, so it requires the appropriate texture mapping to solve the problem [27-28].

1) Color Adjustment

After obtaining the view number corresponding to each triangular face piece, there will be obvious splicing seams at the boundary of the texture color block after projection. The calculated camera parameters are not always accurate, which will lead to the reprojection of the image corresponding to the adjacent triangular face piece being misaligned, which will lead to residual shadows.

Specifically, the steps for global color correction are as follows: first, it must be ensured that each vertex belongs to only one texture color block. Therefore, each vertex on the seam is copied into two vertices. Vertex v_{left} belongs to the triangular facet on the left side of the seam, and v_{right} belongs to the triangular facet on the right side of the seam, at which point each vertex v has a unique color before being adjusted f_v. After that minimization of Eq. (19) computes a color correction term g_v for each vertex:

$$\arg\min_{g} \sum_{v_{kff}, v_{right}} \left(f_{v_{keft}} + g_{v_{kft}} - \left(f_{v_{right}} + g_{v_{right}} \right) \right)^2 + \frac{1}{\lambda} \sum_{v_i, v_j} \left(g_{v_i} - g_{v_j} \right)^2 \tag{19}$$

Where v_i, v_j are adjacent vertices within the same color block. The first term ensures that the adjusted color $\left(f_{v_{left}} + g_{v_{lef}} \right)$ near the left is as similar as possible to the color $\left(f_{v_{right}} + g_{v_{righ}} \right)$ on the right. The second term is used to minimize the difference in color adjustment between adjacent vertices within the same texture color block, which facilitates gradual color adjustment in texture mapping.

The following describes the content of the center of gravity coordinates needed to interpolate the color correction term inside the texture color block corresponding to the triangular face piece. Given the coordinates of the three vertices of triangle ABC, point (x, y), which lies inside the triangle, can be written in the form of a linear combination of the three vertices of triangle ABC, denoted:

$$\begin{gathered} (x, y) = \alpha A + \beta B + \gamma C \\ \alpha + \beta + \gamma = 1 \end{gathered} \tag{20}$$

At this point, (α, β, γ) is said to be the center of gravity coordinate of point (x, y), and since it is inside the triangle, each value of the center of gravity coordinate is positive, e.g., the center of gravity coordinate of point A is $(1, 0, 0)$. The solution for the center of gravity coordinate can be based on the ratio of the geometric areas of each of the triangles, and the point inside the triangle divides the triangle into three small triangles with areas of A_A, A_B, and A_C.

The corresponding coordinates of the center of gravity are calculated as:

$$\begin{aligned} \alpha &= \frac{A_A}{A_A + A_B + A_C} \\ \beta &= \frac{A_B}{A_A + A_B + A_C} \\ \gamma &= \frac{A_C}{A_A + A_B + A_C} \end{aligned} \tag{21}$$

With the help of linear algebra triangle area calculation, the above equation can be transformed into:

$$\begin{aligned}\alpha &= \frac{-(x-x_B)(y_C-y_B)+(y-y_B)(x_C-x_B)}{-(x_A-x_B)(y_C-y_B)+(y_A-y_B)(x_C-x_B)}\\ \beta &= \frac{-(x-x_C)(y_A-y_C)+(y-y_C)(x_A-x_C)}{-(x_B-x_C)(y_A-y_C)+(y_B-y_C)(x_A-x_C)}\\ \gamma &= 1-\alpha-\beta\end{aligned} \tag{22}$$

For practical use, you can use the center of gravity coordinates to interpolate inside the triangle based on known attributes of the three vertices, such as RGB values, texture coordinates, etc. The formula is:

$$V = \alpha V_A + \beta V_B + \gamma V_C \tag{23}$$

In this paper, the interpolated value is the color correction term, which is substituted to obtain the color correction value inside each texture color block. Finally, the correction value is added to the texture color block to form a new texture color block, which is packed into the texture map, and the corresponding texture coordinates are attached to each vertex.

2) Local Poisson Fusion

Even with global color adjustment, seams between adjacent texture color blocks cannot be eliminated. Therefore, after performing global color adjustment, this paper additionally performs local Poisson fusion.

Only f of the above variables is a function of the function to be solved, i.e., the fused image itself. The goal of fusion is to have f such that the fused image overshoots the boundary in a very natural way. The authors of the Poisson image editor proved that the essence of this problem is to solve the following variational problem:

$$\min_f \iint_\Omega |\nabla f - v|^2 \ \textit{with} \ f|_{\partial\Omega} = f^*|_{\partial\Omega} \tag{24}$$

Where ∇f refers to the gradient of the image function f:

$$\nabla = \left[\frac{\partial_n}{\partial x}, \frac{\partial_n}{\partial y}\right] \tag{25}$$

v is the guidance vector field, which here refers to the gradient of the source image. Eq. (24) means that within the fusion region, the gradient of f is the same as the gradient of the source image, and at the boundary location of the fusion region, the value of f is the same as the value of the target image f^*. The solution of Eq. (24) agrees with the solution of Poisson's equation of Eq. (26) at Dirichlet boundary conditions. Namely:

$$\Delta f = \textit{divv over } \Omega, \textit{ with } f|_{\partial\Omega} = f^*|_{\partial\Omega} \tag{26}$$

Definition of gradient based on linear algebra:

$$v = (u, v) = \nabla g \tag{27}$$

Definition of dispersion:

$$divv = \frac{\partial u}{\partial x} + \frac{\partial v}{\partial y} \tag{28}$$

Laplace's definition:

$$\Delta f = \frac{\partial^2 f}{\partial x^2} + \frac{\partial^2 f}{\partial y^2} \tag{29}$$

Based on the above definition, the scatter can be converted to Laplacian:

$$\begin{aligned} divv &= \frac{\partial u}{\partial x} + \frac{\partial v}{\partial y} \\ &= \frac{\partial^2 g}{\partial x^2} + \frac{\partial^2 g}{\partial y^2} \\ &= \Delta g \end{aligned} \tag{30}$$

Thus, the Poisson equation (26) can be transformed into a Laplace filtering result for f that is equal to the Laplace result for g, corresponding to Eq:

$$\Delta f = \Delta g over \Omega, with f\big|_{\partial\Omega} = f^*\big|_{\partial\Omega} \tag{31}$$

The Laplace operator is defined as:

$$\begin{bmatrix} 0 & 1 & 0 \\ 1 & -4 & 1 \\ 0 & 1 & 0 \end{bmatrix} \tag{32}$$

The formula is:

$$4f_p - \sum_{q \in N_p} f_q = 4g_p - \sum_{q \in N_p} g_q \tag{33}$$

Where f_p, g_p denote the current pixel and f_q, g_q denote the neighboring pixels. It is sufficient to express Eq. (33) in matrix form to solve f directly.

In this paper, we limit the Poisson fusion of color blocks to a 20-pixel wide border strip, where fusing only the strip has higher time and memory efficiency than fusing the entire color block. The outer and inner edges of this strip are used as boundary conditions for the Poisson equation. The value of each outer edge pixel is fixed to be the average of the pixel colors in the image corresponding to the color block and the image corresponding to adjacent color blocks, and the value of each inner edge pixel is fixed to its current color. If the color block is too small, the inner edge is left out. To obtain the

bootstrap vector field for the Poisson equation, it is necessary to use the Laplace equation for the border strip.

For all texture color blocks, linear equations are solved in parallel using the open-source library Eigen. The factorization is computed once for each color block and used for all color channels, as the equation's matrix remains constant. Using this method, local Poisson fusion color adjustment can be accomplished, which further eliminates the unnatural excesses of the texture on both sides of the seams and improves the tonal consistency of the texture on the basis of the global color correction.

3 Display design in the new media environment - digital display

3.1 Digital display design

With the application of virtual reality technology, digital interactive technology, multimedia, and other digital technologies in display design, the modern display design concept has broken through the traditional idea of display. More humanized digital display design mode will represent the development direction of display and exhibition.

Digital display design is under the support of new media technology, digital theory as a guide to display design knowledge as a basis, the use of computers, networks, and other new media means, engaged in a variety of display activities to achieve the purpose of display.

The computer-based digital display design is distinct from the traditional physical display. The research scope of digital display design can be divided into the digitalization of physical and virtual displays.

3.2 Virtual reality visualization display based on the new media environment

3.2.1 Virtual Reality Presentation with 3D Modeling

Virtual reality display design based on three-dimensional modeling refers to the three-dimensional scene and three-dimensional object model as the basis, generally with the help of professional modeling software to complete. This modeling method can be more convenient and real performance of real real-world scenes and objects, but it can also generate animation.

Currently the mainstream three-dimensional modeling software such as 3DSMAX, MAYA, etc. Scene and object modeling, mapping, and rendering can be done. This virtual reality display is more powerful and richer.

3.2.2 Design Steps for Virtual Reality Display with 3D Modeling

The design principle of virtual reality display based on three-dimensional modeling is that according to the needs of the display, through a variety of modeling software, geometric entities to construct virtual environments, and movement, mapping, and rendering processing in line with the conditions of virtual reality technology. At present, the mainstream three-dimensional modeling software such as 3DSMAX, MAYA, etc. Can perform scene and object modeling, mapping, and rendering. Then, it was imported into the virtual reality production software to realize interactive operation, and finally, multimedia information integration and output applications.

1) Three-dimensional modeling

According to the purpose of display design, the designer uses 3D modeling software to design and produce 3D digital models and carry out relevant optimization.

2) Production of material mapping, rendering

Create texture material or texture mapping for the designed and produced 3D model and set up scene lighting. According to the requirements of different VR software, adjust the relevant parameters accordingly.

3) Animation production

Produce the corresponding animation effects and set the scene camera.

4) Interactive production

After completing the above design and output, save it as the corresponding format, import it into VR software for editing, realize interactive operation, and add multimedia information such as sound effects, text, navigation interface, etc.

5) Output Release

The virtual design work is completed. Select the type of release for output and put it into practical application.

4 Visualization of three-dimensional images in the new media environment

4.1 Artifact profiling and quality evaluation in 3D image reconstruction

The purpose of the research in this section is to discuss the artifact shape and quality evaluation in 3D image reconstruction algorithms based on face-drawing design, to analyze the data in conjunction with the world-recognized Herman model and Sheep-Logan model, and to propose new quantitative analysis indexes.

4.1.1 Reconstructing artifacts in images

In the inverse projection process, a data point of the projection is made to correspond to a line of the image, which makes the error of the projection process not to be precisely localized. The error of the measurement data is often amplified in the reconstruction of the image so that there is a high probability of artifacts generated by the CT device.

In general, artifacts in CT images can be broadly categorized into four main groups: streak artifacts, shadow artifacts, ring and strip artifacts, and blending artifacts.

4.1.2 Quality evaluation of reconstructed images

To objectively and quantitatively evaluate the effectiveness of the algorithms and the quality of the reconstructed images, the widely recognized Herman model and the Sheep-Logan model are used as research objects.

In this paper, the concept of final measurement accuracy is borrowed and applied to the quality evaluation of reconstructed images, assuming that p denotes the original model, r denotes the

reconstructed image, and $\overline{p}$ denotes the average value of pixels in the original model p. The size of the matrices p, r, and $\overline{p}$ are all $m \times n$. The following three distance metrics are used as measures for quality evaluation.

Normalized root mean square distance:

$$d_1 = \sqrt{\frac{\sum_{i=1}^{n}\sum_{j=1}^{m}\left(p_{i,j} - r_{i,j}\right)^2}{\sum_{i=1}^{n}\sum_{j=1}^{m}\left(p_{i,j} - \overline{p}\right)^2}} \tag{34}$$

Normalized absolute mean distance:

$$d_2 = \frac{\sum_{i=1}^{n}\sum_{j=1}^{m}\left|p_{i,j} - r_{i,j}\right|}{\sum_{i=1}^{n}\sum_{j=1}^{m}\left|p_{i,j}\right|} \tag{35}$$

Corresponds to the farthest distance of the pixel (2×2 area):

$$d_3 = \max_{\substack{1 \le k \le [n/2] \\ 1 \le l \le [m/2]}} \left(\left|P_{k,l} - P_{k,l}\right|\right) \tag{36}$$

4.1.3 Image reconstruction results

The statistical results of the images derived from the reconstruction of the Herman model and the Sheep-Logan model are shown in the table below. The common Hamming, Hanning, and Cosine filters are used for the experiments, and the results of the parallel beam inverse projection reconstruction are listed as a comparison.

The Herman model's statistical results can be seen in Fig. 3. The mean values of Hamming filter for the 3D image reconstruction method based on the surface drawing technique proposed in this paper and the parallel beam inverse projection reconstruction method are 0.210215 and 0.211125, respectively. The minimum values of Hanning and Cosine filters are -0.038641 and -0.019365, respectively, and -0.042155 -0.021532.

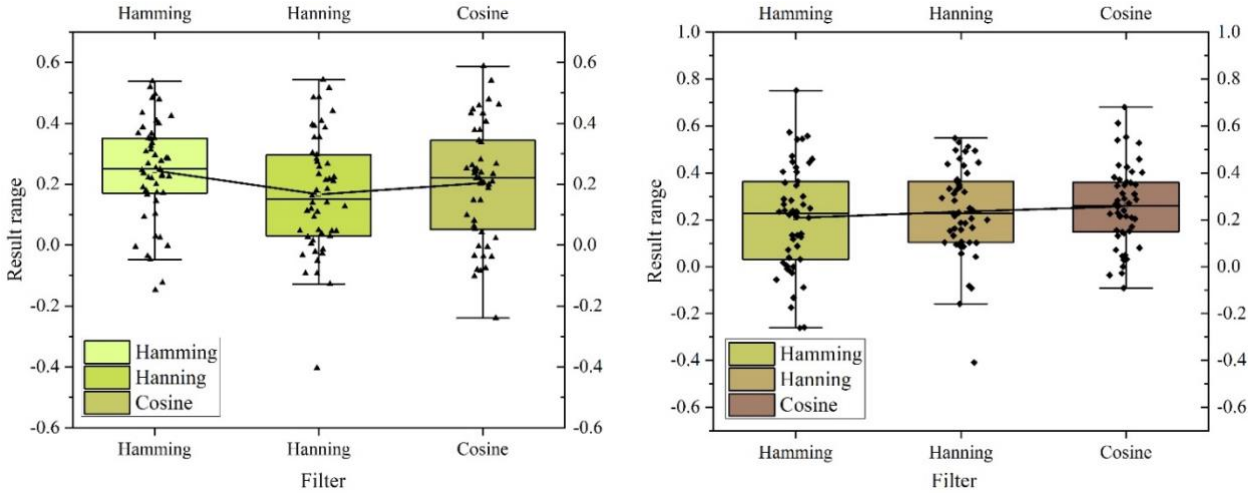

(a) The method reconstruction results (b) Parallel beam inversion reconstruction results

Figure 3. The statistical results of the Herman model

The image statistics of the Sheep-Logan model are shown in Fig. 4. The mean values of the Hamming, Hanning, and Cosine filters for the two reconstruction methods are 0.0602322 vs. 0.0611233, 0.0645317 vs. 0.0601462, and 0.064350 vs. 0.0602127, respectively, and the difference in their mean values is smaller.

In summary, the reconstruction results obtained by the Hamming filter are better, both for the image reconstruction based on the surface-drawing technique used in this paper and for the parallel beam inverse projection reconstruction. The reconstructed Herman model and Sheep-Logan model both exhibit some degree of ring and strip artifacts around the image. Still, the reconstruction accuracy of the central region of the image is relatively high.

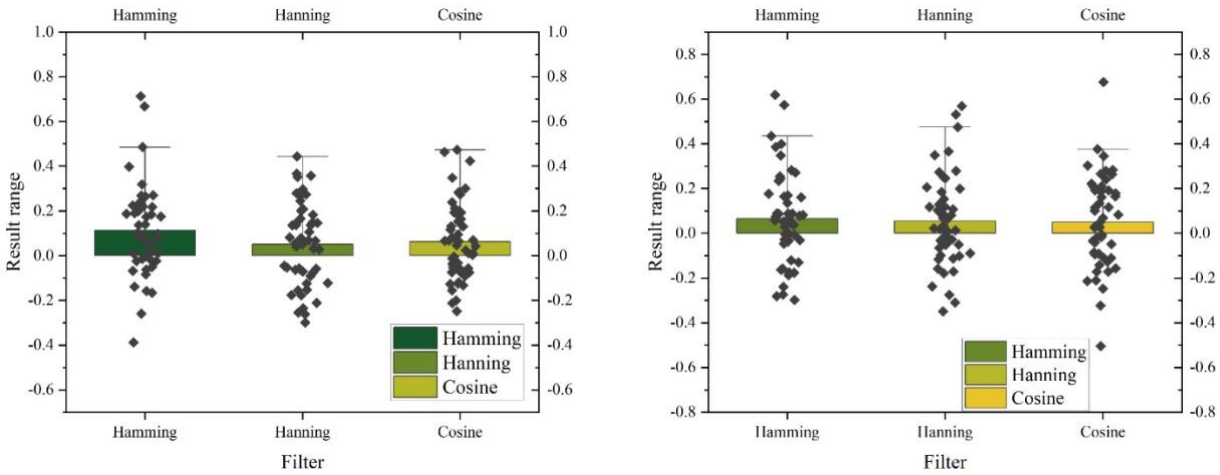

(a) The method reconstruction results (b) Parallel beam inversion reconstruction results

Figure 4. Image statistics of the sheep-logan model

4.2 Dynamic Texture Large Scale Data Field Body Mapping Presentation

In this paper, the algorithm is tested and experimented with a large amount of new media display application data, and the experimental platform is NVIDIA GeForce 7800GT with 256MB video memory, which is realized in C++ and OpenGL.

The performance parameters of the texture drawing algorithm in this paper are shown in Table 1. For different data sizes of the human body image reconstruction target, the drawing algorithm proposed in this paper requires different preprocessing times. Still, none of them is more than 3s, and the frame rate is 3.7fps when the human body data size is 512×512×1638.

Before drawing, the algorithm in this paper requires a certain amount of preprocessing time to complete the chunking operation of the data. When the data is divided into more chunks with a larger scale, the delay of the system in transmitting the data to the graphic hardware exacerbates the overhead of real-time switching of the texture, resulting in a decrease in the drawing frame rate. However, with the dynamic texture loading technique, the occupancy of texture memory in the drawing is independent of the size of the data field, which overcomes the limitations of the graphics hardware on the traditional texture mapping body drawing algorithm and realizes the complete drawing of large-scale data fields.

The ability of the drawing algorithm proposed in this paper to draw large-scale body data is demonstrated by the experimental results. At the same time, since no complex coding algorithm is used to compress the body data, the impact of the time-consuming decoding operation on interactivity in the drawing is avoided, as well as the errors caused by coding and decoding, and high-quality drawing results can be obtained, which improves the scope of application of the body-drawing technology in the actual digital display.

Table 1. Texture drawing algorithm performance parameters

Body data	Data size	Pretreatment(s)	Data block	Frame rate(fps)
Abdomen	$512\times512\times536$	0.98	4	9.1
Spine	$512\times512\times598$	1.02	4	9.2
Human body-1	$512\times512\times690$	1.35	5	8.5
Human body-2	$512\times512\times971$	1.97	5	6.3
Lower limb	$512\times512\times1235$	2.46	6	4.1
Human body-3	$512\times512\times1638$	2.98	7	3.7

4.3 Visualization of the face drawing algorithm

In the VTK new media visualization platform, there is a lack of control mechanism for the number of grid cells and the distance of sampling points, which can not effectively study the influence of the change of the position of sampling points on the 3D reconstruction effect.

We are experimenting to examine the effects of different sampling spacing and grid cell numbers on the 3D reconstruction effect and time when extracting the same isotropic surface.

The data size and the number of images of different tissues are shown in Table 2. The tissues include the nasopharynx, scalp, brain white matter, cerebrospinal fluid, brain gray matter, bone cancellous matter, bone dense matter, and background, and the data size and the number of images of the nasopharynx, for example, are 9.86M and 70 images, respectively. The background-size was 16.8M, and the number of images was 145.

Table 2. Data size and number of images of different organizations

Organization	Data size (M)	Picture number (tensor)
Nasopharyngeal	9.86	70
Scalp	14.2	120
White matter	15.4	130
Cerebrospinal fluid	16.1	135
Gray matter	16.5	135
Osteophyte	16.6	135
Bone density	16.8	140
Background	16.8	145

Combining the tissue data size and the number of images, different sampling intervals were set to analyze the 3D reconstruction time under 64, 128, and 256 sampling intervals. The effect of setting different sampling intervals on the time required for 3D reconstruction is shown in Fig. 5, with the bone densities taking the most time for 3D reconstruction at different sampling intervals, requiring 1435.21ms at 256 sampling intervals, much more than the reconstruction time of other tissues.

Combining the reconstruction time of 3D images, the following conclusions can be obtained.

1) The higher the number of grid cells, the smaller the sampling interval and the denser the sampling points. The basic principle of face drawing is to complete the fitting of the set threshold equivalent face by using triangular face sheets in the grid cells. Therefore, the denser the sampling points, the higher the degree of fitting, the more complete the preservation of equivalent surface information, the more detailed the effect of 3D reconstruction, and the higher the image quality.

2) The denser the sampling points are, the longer it takes to fit the isosurfaces with a set threshold.

3) In order to achieve better real-time performance on the basis of ensuring the quality of the reconstruction effect, the distance of sampling points and the number of grid cells should be set according to the needs.

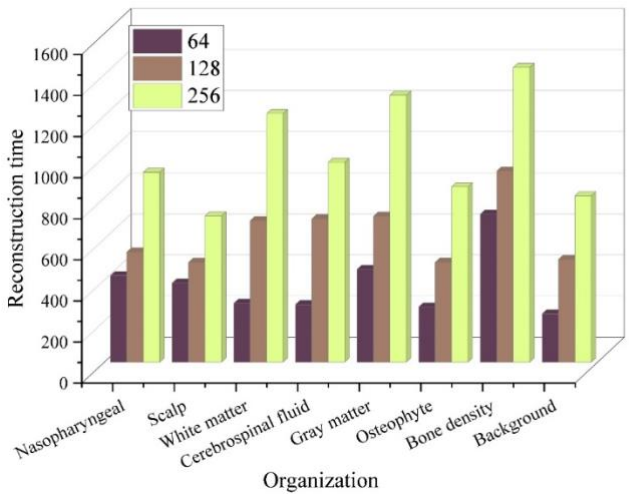

Figure 5. The impact of different sampling intervals on the time of 3d reconstruction

5 Conclusion

This paper proposes a virtual reality visualization display in a new media environment, using visualization technology for 3D image imaging, proposes a texture mapping algorithm to enhance the realism of 3D images to reduce the ghosting phenomenon, and optimizes the visualization display. The virtual reality display scheme designed in this paper is applied to 3D reconstruction and visualization of new media digital images to analyze the visualization presentation effect of these images.

Using the Herman model and the Sheep-Logan model for data analysis, the projection data are reconstructed by inverse projection with different filter functions, and the mean values of the Hamming filters of the three-dimensional image reconstruction method based on the surface drawing technique and the parallel-beam inverse projection reconstruction method are 0.210215 and 0.211125, respectively. The reconstruction results obtained by using the Hamming filters are better.

Combined with the new media digitized display data to test the algorithm experiments, the drawing algorithm proposed in this paper overcomes the limitations of the graphics hardware on the traditional texture mapping body drawing algorithm and realizes the complete drawing of a large-scale data field.

Extracting the same isotropic surface under the condition of different organizations, the three-dimensional reconstruction time of each organization under different sampling intervals is not more than 2s, and the three-dimensional image visualization technology proposed in this paper has strong real-time performance.

References

[1] Hedman, P., & Kopf, J. (2018). Instant 3d photography. ACM Transactions on Graphics, 37(4CD), 1-12.

[2] Zhang, L. (2019). Application research of automatic generation technology for 3d animation based on ue4 engine in marine animation. Journal of Coastal Research, 93(sp1), 652.

[3] Cao, M., Zheng, L., Jia, W., Lu, H., & Liu, X. (2020). Accurate 3-d reconstruction under iot environments and its applications to augmented reality. IEEE Transactions on Industrial Informatics, PP(99), 1-1.

[4] Zhao, H. (2021). Design of sanda action reconstruction model based on 3d images. Wireless Communications and Mobile Computing, 2021(1), 1-6.

[5] Alejandro Beacco · Jaime Gallego · Mel Slater. (2022). 3d objects reconstruction from fronta1 images an examp1e with guitars. The Visual Computer, 1-16.

[6] Zhao, H., & Wu, B. (2020). Three-dimensional face modeling technology based on 5g virtual reality binocular stereo vision. International Journal of Communication Systems.

[7] Wang, J., Zhang, Y., Lei, X., & Wu, Y. (2023). Compact reconstruction of a fourier hologram for a 3d object by scaling compensation. Applied optics, 62 10, 2604-2609.

[8] Xu, L. (2021). Fast modelling algorithm for realistic three-dimensional human face for film and television animation. Complexity, 2021(2), 1-10.

[9] Sun, H., Li, Y., & Paik, J. (2019). Application of vr technology in the optimization modeling of port wave-proof building. Journal of Coastal Research, 97(sp1), 267.

[10] Shi, L., Webb, R., Xiao, L., Kim, C., & Jang, C. (2022). Neural compression for hologram images and videos. Optics Letters.

[11] Leimkuehler, T., & Drettakis, G. (2021). Freestylegan: free-view editable portrait rendering with the camera manifold. ACM Transactions on Graphics.

[12] Qiu, W., Shangguan, W., Chai, L., Cai, B., & Chen, J. J. (2021). Parallel hierarchical control-based efficiency enhancement for large-scale virtual reality traffic simulation. IEEE Intelligent Transportation Systems Magazine, PP(99).

[13] Tang, L., Huang, H., Zhang, Y., Qi, G., & Yu, Z. (2023). Structure-embedded ghosting artifact suppression network for high dynamic range image reconstruction. Knowledge-Based Systems, 263, 110278-.

[14] Stefanou, M., Muryy, A., & Glennerster, A. (2020). A homing task that could not be done by image matching. Journal of Vision, 20, 396.

[15] Li, L. (2022). The influence of digital twins on the methods of film and television creation. Computers and Electrical Engineering.

[16] Tu, Z., Weng, D., Liang, B., & Luo, L. (2022). Expression retargeting from images to three-dimensional face models represented in texture space. Journal of the Society for Information Display.

[17] Kong, S. (2020). 3d image reconstruction of marine plankton based on virtual reality. Journal of Coastal Research, 103, 851 - 854.

[18] Peng, J., Fu, K., Wei, Q., Qin, Y., & He, Q. (2020). Improved multiview decomposition for single-image high-resolution 3d object reconstruction. Wireless Communications and Mobile Computing.

[19] Ebner, T., Feldmann, I., Renault, S., Schreer, O., & Eisert, P. (2017). Multi-view reconstruction of dynamic real-world objects and their integration in augmented and virtual reality applications. Journal of the Society for Information Display, 25(3), 151-157.

[20] Zou, X., He, H., Wu, Y., Chen, Y., & Xu, M. (2020). Automatic 3d point cloud registration algorithm based on triangle similarity ratio consistency. IET Image Processing, 14.

[21] Dong, Y., Wu, H., Yang, X., Chen, X., & Xi, J. (2024). Shape-aware speckle matching network for cross-domain 3d reconstruction. Neurocomputing, 585.

[22] Yu, J., Yin, W., Hu, Z., & Liu, Y. (2023). 3d reconstruction for multi-view objects. Computers & Electrical Engineering, 106, 108567-.

[23] Yu, L., Fu, X., Xu, H., & Fei, S. (2020). High-precision camera pose estimation and optimization in a large-scene 3d reconstruction system. Measurement Science & Technology(8), 31.

[24] Simonov E. N. & Vinogradov K. M.(2023).An algorithm for reconstruction of three-dimensional images in computed X-ray tomography with a cone irradiation beam.Biomedical Engineering(4),271-275.

[25] Jiawei Tian,Botao Ma,Siyu Lu,Bo Yang,Shan Liu & Zhengtong Yin.(2023).Three-Dimensional Point Cloud Reconstruction Method of Cardiac Soft Tissue Based on Binocular Endoscopic Images. Electronics (18),

[26] Guo Shiqi,Yu Tao,Chen Xiuyun,Cui Mingming,Liu Dingsheng,Xu Shuo.. & Zhang Hong. (2023). Variations of the double superior mesenteric vein are not rare: An observational study using computed tomography, three-dimensional image reconstruction, and surgery.European journal of surgical oncology : the journal of the European Society of Surgical Oncology and the British Association of Surgical Oncology(10),106972-106972.

[27] Malone Brendan & Searle Ross.(2021).Updating the Australian digital soil texture mapping (Part 1*): re-calibration of field soil texture class centroids and description of a field soil texture conversion algorithm.SOIL RESEARCH(5),419-434.

[28] Wang Wensheng & Su Chang.(2022).An optimization method for motion blur image restoration and ringing suppression via texture mapping.ISA transactions650-661.

About the Author

Yige Sun was born in Baoding, Hebei, P.R. China, in 1988. He received the bachelor's degree from Communication University of Zhejiang, P.R. China, and master's degree from Pratt Institute, the

United States. Now, he works as a lecturer of Animation in HBU-UCLan School of Media, Communication and Creative Industries, Hebei University. His research interest includes virtual reality, 3D animation and digital arts.

Zixuan Zhang was born in Xingtai, Hebei, P.R. China, in 2002. Now, she is studying advertising at HBU-UCLan School of Media, Communication and Creative Industries in Hebei University, P.R. China. Her research interests include new media operations and virtual reality interaction.

Nan Yan was born in Baoding, Hebei, P.R. China, in 1988. She received the Master degree from Leicester University, UK. Now, she works as lecturer in HBU-UCLan School of Media, Communication and Creative Industries in Hebei University. Her research interests includes new media and communication strategy.